Journal of Materials Chemistry B

ROYAL SOCIETY OF CHEMISTRY

PAPER

View Article Online
View Journal | View Issue

Cite this: J. Mater. Chem. B, 2021, 9, 7216

Engineering $Cu_{2-x}S$-conjugated upconverting nanocomposites for NIR-II light-induced enhanced chemodynamic/photothermal therapy of cancer†

Kaimin Du,[ab] Shuang Zhao,[a] Jing Feng,*[ab] Xuan Gao,[ab] Kai Liu,[ac] Xiaozhen Wang,*[d] Manli Zhang,[ab] Yao Li,[ab] Yu Lu[a] and Hongjie Zhang*[abc]

Received 17th February 2021,
Accepted 22nd March 2021

DOI: 10.1039/d1tb00337b

rsc.li/materials-b

The integration of chemodynamic therapy (CDT) and photothermal therapy (PTT) has played a huge role in improved anticancer treatments. Here, a novel multifunctional nanoplatform based on $Cu_{2-x}S$ conjugated $NaYF_4$:Yb/Er@$NaYF_4$:Yb upconversion nanoparticles (UCNPs) was proposed and designed. In the UCNPs–$Cu_{2-x}S$ nanocomposites, UCNPs with excellent luminescent properties and a high X-ray attenuation coefficient can serve as an upconversion luminescence (UCL) and computer tomography (CT) imaging contrast agent; meanwhile, Cu(II) in the $Cu_{2-x}S$ nanodots enables the nanocomposites to have a magnetic resonance imaging (MRI) ability owing to the presence of unpaired electrons. Moreover, the $Cu_{2-x}S$ nanodots with a strong absorbance in the NIR II biowindow not only could be employed as a stable photothermal agent under NIR laser irradiation, but also could be used as a photothermal-enhanced Fenton nanocatalyst to respond to over-expressed H_2O_2 in the tumor microenvironment (TME) and generate toxic hydroxyl radicals (•OH) to effectively kill cancer cells. Furthermore, the UCNPs–$Cu_{2-x}S$ nanocomposites possess negligible cytotoxicity and a high photothermal conversion efficiency (43.8%) in the NIR-II biowindow (1064 nm), indicating that they possess great potential for the UCL/CT/MR multi-modal imaging guided synergistic enhanced CDT/PTT of cancer.

Introduction

As is known, the diagnosis and therapy of cancer remains an urgent problem and requires researchers to continuously develop efficient theranostic agents for the more accurate diagnosis and treatment of cancer.[1–6] Recently, various therapy techniques such as photodynamic therapy (PDT),[4,7–9] photothermal therapy (PTT),[10–13] chemodynamic therapy (CDT),[14–16] radiotherapy (RT)[3,17] and chemotherapy[18–20] guided by multimodal imaging have played pivotal roles. Among them, PTT, which absorbs near-infrared (NIR) light by photoabsorbing materials and converting it into hyperthermia to eliminate tumor cells, has been widely applied in the field of anticancer therapy owing to its unique advantages such as low systematic toxicity, remote-control properties and high selectivity. Numerous photothermal agents including precious metal gold (Au) or platinum (Pt) nanoparticles,[21,22] carbon nanomaterials,[23] metal chalcogenides (such as CuS nanoparticles, $Cu_{2-x}Se$ nanoparticles, Bi_2Se_3 nanosheets or MoS_2 nanosheets)[24–27] polymeric nanoparticles[28] *etc.* have been widely used in PTT owing to their outstanding photothermal conversion performance of transferring NIR optical energy into heat. However, single-modal therapy cannot completely eradicate malignant tumors due to the complexity and diversity of the tumor environment. The combination of multiple treatment methods can overcome the weakness of each treatment tool, achieving the synergistic and efficient treatment of cancer.[29] CDT as an emerging treatment modality, which uses Fenton-like reactions to generate the highly cytotoxic hydroxyl radical (•OH), has aroused great research interest. Fe-based nanomaterials are still the most commonly used CDT agents; however, their applications are greatly limited by the narrow working pH range and slow reaction rate of the Fenton reaction.[15] Particularly, $Cu_{2-x}S$ nanoparticles have attracted considerable attention due to their intriguing merits of ultrasmall size, synthetic simplicity, low cost, low cytoxicity, biodegradability, strong absorbance in the NIR II region,

[a] State Key Laboratory of Rare Earth Resource Utilization, Changchun Institute of Applied Chemistry, Chinese Academy of Sciences, 5625 Renmin Street, Changchun 130022, China. E-mail: fengj@ciac.ac.cn, hongjie@ciac.ac.cn; Fax: +86 431 85698041; Tel: +86 431 85262127
[b] University of Science and Technology of China, Hefei 230026, China
[c] Department of Chemistry, Tsinghua University, Beijing 100084, China
[d] The first hospital of Jilin University, Changchun 130021, China. E-mail: xzwang@jiu.edu.cn

† Electronic supplementary information (ESI) available: Supplementary figures and table of the characterizations of the as-prepared nanoparticles. See DOI: 10.1039/d1tb00337b

as well as their high photothermal conversion efficiency, which make them promising candidates for potent PTT. What is more meaningful to us is that Cu(I)-based $Cu_{2-x}S$ nanodots could serve as an efficient nanocatalyst, responding to the over-expressed H_2O_2 in the tumor microenvironment (TME) and generating toxic $^{\bullet}OH$ for the effective killing of cancer cells.[30]

Importantly, a prerequisite for the effective treatment of cancer is early accurate positioning and tracking of the tumor. As a non-invasive imaging technology, magnetic resonance imaging (MRI) has high temporal and spatial resolution and an extremely high tissue penetration depth. Recently, it has been reported that paramagnetic Cu(II) can be used as a T_1 contrast agent.[15,31,32] Pan *et al.* synthesized a copper-based contrast agent for high-resolution MRI. The reagent provides strong T_1 contrast *in vitro* and can be used to diagnose unstable plaque rupture in palpable vascular structures.[32] Our group synthesized high-efficiency Cu(I)-based Cu_3P NCs for *in situ* MRI due to the generation of paramagnetic Cu(II) in response to the excess H_2O_2 in the TME.[15] However, single modality imaging may not provide the evidence needed for accurate tumor diagnosis. Of the current diagnosis modalities, the X-ray CT imaging technique, with excellent spatial and density image resolution together with deep tissue penetration, has been extensively used in modern clinical diagnosis and treatment monitoring.[11,13] Compared with MR and CT imaging, optical imaging with real-time dynamic imaging capabilities has drawn immense attention. Therefore, a more accurate diagnosis could be achieved through a combination of multiple imaging modes. As is known, lanthanide ion (Ln^{3+})-doped upconversion nanoparticles (UCNPs) with notable merits such as large anti-Stokes shifts, negligible auto-fluorescence, excellent detection sensitivity, high penetration depth and good biocompatibility have the ability to emit UV, visible and NIR light under NIR laser irradiation, which make them promising candidates for visual tracking in the theranostic field.[33,34] Therefore, UCNPs can be selected as promising candidates for potential applications in biological labeling,[35,36] biological imaging,[37,38] sensing[7,39] and clinical therapeutics.[40,41] Up to now, considerable efforts have been devoted to the synthesis of nanocomposites based on UCNPs and CuS nanodots through specific chemical or physical combinations, which could provide extensive potential for the synergistic diagnosis and treatment of tumor.[3,42] However, the synthesis processes are somewhat time-consuming and physical adsorption is unstable. Moreover, there is a paucity of research on the construction of UCNPs-based nanocomposite platforms with $Cu_{2-x}S$ as a good imaging agent, excellent nanocatalyst and photothermal agent for the accurate diagnosis and treatment of cancer.

In this work, we prepared multifunctional UCNPs–$Cu_{2-x}S$ nanocomposites for the UCL/CT/MR multi-modal imaging-guided synergistic enhanced CDT/PTT of cancer. Firstly, oleic acid-modified $NaYF_4$:Yb/Er@$NaYF_4$:Yb nanoparticles (OA-UCNPs) were obtained through a solvothermal process. Then, hydrophobic UCNPs were hydrolyzed by coating with chitosan (CS). Finally, ultrasmall water-soluble $Cu_{2-x}S$ nanodots were grown uniformly on the surface of the UCNPs. It is found that the resultant UCNPs–$Cu_{2-x}S$ nanoplatform retains the real-time dynamic monitoring UCL imaging properties of the UCNPs and shows great promise in CT imaging owing to the high X-ray attenuation coefficient of the Yb element. Meanwhile, UCNPs–$Cu_{2-x}S$ could act as a contrast agent for MRI owing to the existence of Cu(II) in the $Cu_{2-x}S$ nanodots. Moreover, the Cu(I)-based $Cu_{2-x}S$ nanodots could not only generate toxic $^{\bullet}OH$ to respond to over-expressed H_2O_2 in the TME, but also possess excellent photothermal lethality under 1064 nm laser irradiation. *In vitro* and *in vivo* assays proved that the nanocomposites possess favorable biocompatibility, negligible toxicity, a high photothermal conversion efficiency, excellent photothermal stability, an outstanding photothermal killing effect and a PT-enhanced CDT effect, showing great potential as ideal UCL/CT/MR multi-modal imaging-guided CDT/PTT agents.

Experimental procedures

Materials

Yttrium chloride ($YCl_3 \cdot 6H_2O$, 99.9%), ytterbium chloride ($YbCl_3 \cdot 6H_2O$, 99.99%), erbium chloride ($ErCl_3 \cdot 6H_2O$, 99.99%), oleic acid (OA, 90%), 1-octadecene (ODE, 90%), chitosan (CS, deacetylation degree $\geq$95%, viscosity: 100–200 mPa·s) were purchased from Aladdin Reagents. Sodium sulfide (Na_2S), sodium citrate (Na_3Cit), cetyltrimethylammonium bromide (CTAB, 99%), sodium hydroxide (NaOH, >98%), ammonium fluoride (NH_4F), methanol (CH_3OH), ethanol (C_2H_5OH), cyclohexane, and copper chloride ($CuCl_2$), were obtained from Beijing Chemical Reagents Materials. All chemical reagents are of analytical grade and were used without any further purification.

Measurements

Powder X-ray diffraction (XRD) data were measured on a Bruker D8 Focus powder X-ray diffractometer at a scanning rate of 0.5° min^{-1} in the 2θ range from 10 to 70° using Cu Kα radiation (λ = 1.5418 Å) at an operating voltage of 40 kV and a current of 40 mA. Transmission electron microscopy (TEM), high-resolution transmission electron microscopy (HRTEM), bright-field TEM and the corresponding EDX elemental mapping images were obtained on a FEI Tecnai G2S-Twin instrument with a field emission gun operating at 200 kV. The composition of the samples was studied using a field emission scanning electron microscope (FE-SEM, S-4800, Hitachi) equipped with an energy-dispersive X-ray (EDX) spectrometer. X-ray photoelectron spectroscopy (XPS) were conducted with a VGESCALAB MKII spectrometer. The absorption spectrum was measured using a Shimadzu UV-3600 UV-vis-NIR spectrophotometer. The chemical compositions were determined by inductively coupled plasma optical emission spectrometry (ICP-OES, with a Varian Liberty 200 spectrophotometer). The UCL spectra were recorded using a 980 nm laser diode and a triple grating monochromator (Spectra Pro-2758, Acton Research Corporation) equipped with a photomultiplier (Hamamatsu R928).

Synthesis of OA-stabilized core–multishell $NaYF_4$:Yb,Er@$NaYF_4$:Yb nanoparticles (labeled as UCNPs)

First, OA-capped $NaYF_4$:Yb/Er (Y : Yb : Er = 80 : 18 : 2 (molar ratio)) core nanoparticles (NPs) were synthesized according to the literature

methods.[43] The resulting core NPs were purified by centrifugation after the addition of ethanol, washed several times with cyclohexane and ethanol, and finally re-dispersed in cyclohexane for subsequent shell growth. Briefly, the as-prepared $NaYF_4$:Yb/Er core NPs (1 mmol), CF_3COONa (1 mmol), $Y(CF_3COO)_3$ (0.6 mmol), and $Yb(CF_3COO)_3$ (0.4 mmol) were added to a mixture of OA (6.5 mL) and ODE (6.5 mL) in a three-necked flask at room temperature. The solution was pre-degassed for 10 min under vigorous stirring and then heated to 100 °C for 30 min to form a transparent solution and remove residual water under an argon atmosphere. After that, the temperature was increased to 300 °C and maintained for 60 min under an argon atmosphere. Finally, the resulting nanoparticles were purified by centrifugation, washed several times with cyclohexane and ethanol, and finally re-dispersed in cyclohexane for further experiments.

Synthesis of chitosan-functionalized UCNPs (CS-UCNPs) and UCNPs–$Cu_{2-x}S$ nanocomposites

The CS layer was coated on the surface of the UCNPs with the assistance of CTAB to transfer the hydrophobic UCNPs into the aqueous phase. CS-UCNPs were synthesized according to our previously reported method.[44] Then, the UCNPs–$Cu_{2-x}S$ nanocomposites were synthesized through an *in situ* growth routine. First, 1 mL of the synthesized CS-UCNPs nanoparticles were diluted to 10 mL with deionized water, followed by the addition of $CuCl_2$ solution (10.0 mM, 1 mL) and then the mixture was stirred at room temperature for more than 2 h. Finally, Na_3Cit solution (0.5 M), and then Na_2S (0.1 M) were added to the mixture drop by drop. After the reactant was stirred at room temperature for 5 min, the solution was kept at 90 °C for 15 min. After that, the solution was put into ice water and kept cold for further use.

Photothermal properties of UCNPs–$Cu_{2-x}S$ nanocomposites

UCNPs–$Cu_{2-x}S$ nanocomposite aqueous solutions with different Cu concentrations (0, 12.5, 25, 50, 100, 200 μg mL^{-1}) were exposed to 808 nm and 1064 nm laser irradiation (1.0 W cm^{-2}, 10 min), respectively. The solution temperature was measured every 10 s by a thermocouple microprobe. To deduce the photothermal conversion efficiency (η), the UCNPs–$Cu_{2-x}S$ (200 μg mL^{-1}) aqueous solution was irradiated with an NIR laser until the temperature was steady. Then, the laser was turned off and the system temperature was cooled naturally to ambient temperature with measuring of the temperature every 10 s. The η value was calculated using eqn (1)–(4):

$$\eta = hS(T_{max,NPs} - T_{max,solvent})/I(1 - 10^{-A_{808\text{ or }1064}}) \quad (1)$$

$$\tau_s = m_d C_d/hS \quad (2)$$

$$t = -\tau_s \ln \vartheta \quad (3)$$

$$\vartheta = T - T_{surr}/(T_{max,nanocomposites} - T_{max,solvent}) \quad (4)$$

where h is the heat transfer coefficient, S is the surface area of the container, $T_{max,nanocomposites}$ and $T_{max,solvent}$ are the maximum steady-state temperatures of the UCNPs–$Cu_{2-x}S$ nanocomposites solution and water, which are 64.6 and 22.6 °C for 808 nm laser irradiation, and 75.7 and 23.5 °C for 1064 nm laser irradiation, respectively. I is the incident laser power (1.0 W cm^{-2}), and $A_{808\text{ or }1064}$ is the absorbance of the UCNPs–$Cu_{2-x}S$ nanocomposites at 808 nm (A_{808} = 0.68) or 1064 nm (A_{1064} = 1.35). τ_s is the sample system time constant, and m_d and C_d are the mass (1.0 g) and heat capacity (4.2 J g^{-1}), respectively, of the deionized water used as the solvent. θ is the dimensionless driving force temperature, T_{surr} is the ambient temperature of the surroundings, T is a temperature of the UCNPs–$Cu_{2-x}S$ aqueous solutions at a constant cooling time (t), the value of $\tau_{s,808}$ was determined to be 189.68 s (Fig. S11, ESI†) and $\tau_{s,1064}$ was determined to be 180.60 s (Fig. 2d). The photothermal conversion efficiency of the UCNPs–$Cu_{2-x}S$ nanocomposites was calculated according to eqn (5):

$$\eta = m_d C_d(T_{max,nanocomposites} - T_{max,H_2O})/I(1 - 10^{-A_{808\text{ or }1064}})\tau_s. \quad (5)$$

Detection of extracellular •OH

Briefly, UCNPs–$Cu_{2-x}S$ nanocomposites (200 μg mL^{-1}) were added in 2 mL of MB oxygen-free solution (10 mg L^{-1}) at pH 6.5 or pH 7.5 to establish an adsorption/desorption. After stirring for 2 h, different concentrations of H_2O_2 (0.5, 1, 2 mM) was added to the mixture, and the degradation of MB was evaluated by UV-visible absorption spectroscopy. In the same way, the effect of temperature to •OH production was evaluated by 1064 nm laser irradiation.

In vitro cytotoxicity assay

Typical cell counting kit 8 (CCK-8) assays were performed to assess the cytotoxicity of the UCNPs–$Cu_{2-x}S$ nanocomposites. In detail, HeLa cells were first put in a 96-well plate (about 5000 per well) and cultured at 37 °C and 5% CO_2 for 24 h in DMEM supplemented with 10% FBS. Then, the cells were washed with PBS and incubated with UCNPs–$Cu_{2-x}S$ nanocomposites at different Cu concentrations (0, 12.5, 25, 50, 100, 200 μg mL^{-1}) at 37 °C incubated for another 12 h and 24 h. Then, the cell viabilities were detected by the CCK-8 assay. The absorption of each solution was measured at 450 nm on a microplate reader (Thermo, Varioskan Flash).

In vitro synergistic enhanced CDT and PTT of UCNPs–$Cu_{2-x}S$ nanocomposites

To evaluate the synergistic enhanced CDT and PTT for the killing of cancer cells, HeLa cells were first put in a 96-well plate (about 5000 per well) and cultured at 37 °C and 5% CO_2 for 24 h in DMEM supplemented with 10% FBS. To assess the synergistic cytotoxicity, each group was treated with different approaches including a control, the 1064 nm laser only, UCNPs–$Cu_{2-x}S$ only (Cu concentration = 200 μg mL^{-1}), UCNPs–$Cu_{2-x}S$ (Cu concentration = 100 and 200 μg mL^{-1}) + H_2O_2 (100 μM), UCNPs–$Cu_{2-x}S$ (Cu concentration = 100 and 200 μg mL^{-1}) + laser, UCNPs–$Cu_{2-x}S$ (Cu concentration = 200 μg mL^{-1}) + H_2O_2 (100 μM), followed by 1064 nm laser irradiation (6 min). Finally, the cell viabilities were detected by the CCK-8 assay.

Intracellular •OH production

HeLa cells were first put in a 24-well plate and cultured at 37 °C and 5% CO_2 for 24 h in DMEM supplemented with 10% FBS. Then, the cells were washed with PBS and new culture media (pH = 6.5, 100 μM of H_2O_2) containing UCNPs–$Cu_{2-x}S$ nanocomposites (Cu concentrations = 200 μg mL^{-1}) was added. (pH = 6.5, 100 μM of H_2O_2) containing UCNPs–$Cu_{2-x}S$ nanocomposites (Cu concentrations = 200 μg mL^{-1}) and incubated at 37 °C for another 24 h. Then, cells were washed with PBS and irradiated with the 1064 nm laser (1.0 W cm^{-2}) for 6 min. The fluorescence intensity of each well was measured by fluorescence microscope.

In vitro photothermal effect of UCNPs–$Cu_{2-x}S$ nanocomposites

The cell live/dead assays were carried out to evaluate the efficiency of PTT. Briefly, HeLa cells seeded into a 24-well plate were divided into four groups (1–4) as follows: (1) control group (PBS solution), (2) 1064 nm laser only group (1064 nm, 1.0 W cm^{-2}, 6 min), (3) UCNPs–$Cu_{2-x}S$ (Cu = 200 μg mL^{-1}) + 100 μM H_2O_2 group, and (4) UCNPs–$Cu_{2-x}S$ (Cu = 200 μg mL^{-1}) + 100 μM H_2O_2 + 1064 nm laser (1.0 W cm^{-2}, 6 min) group. A mixed solution containing 2 μM of calcein (AM) and 8 μM of propidium iodide (PI) was then added to the wells. After being stained for 40 min, the cells were washed with PBS and examined using a fluorescence microscope to detect the live/dead status.

In vitro UCL imaging of UCNPs–$Cu_{2-x}S$ nanocomposites

The *in vitro* upconversion luminescence imaging of HeLa cells was carried out by a custom-built instrument for upconversion luminescence microscopy, which was rebuilt from an inverted fluorescence microscope (Nikon Ti–S) with an external laser diode for illuminating the samples. HeLa cells were seeded in 24-well culture plates (4×10^4 cells per well) and incubated (37 °C, 5% CO_2) overnight. Then, the original cell culture medium was discarded and fresh culture medium containing UCNPs–$Cu_{2-x}S$ solution (200 μg mL^{-1}, 0.5 mL) was added into each well and incubated at 37 °C for 2 h, 6 h, 12 h and 24 h. Then, the cells were carefully washed with PBS three times, fixed with 4% paraformaldehyde PBS solution for 15 min and then use an inverted fluorescence microscope equipped with a 980 nm laser to observe the UCL imaging effect of UCNPs-$Cu_{2-x}S$ in cells.

Animal experiments

Balb/c mice were purchased from the Laboratory Animal Center of Jilin University (Changchun, China). Animal care and handing procedures were in adherence with the guidelines of the Regional Ethics Committee for Animal Experiments. The tumor models were established by subcutaneous injection of U14 cells in the left axilla of each mouse. The tumor-bearing mice were used for experiments when the tumor size had reached about 100–200 mm^3.

In vitro and *in vivo* CT and MR imaging of UCNPs–$Cu_{2-x}S$ nanocomposites

For *in vitro* CT imaging, the CT contrast efficacy of UCNPs–$Cu_{2-x}S$ nanocomposites was compared with clinical iobitridol using the same element concentrations of 0, 0.31, 0.63, 1.25, 2.5, 5.0, 10.0 mg mL^{-1}. For *in vivo* CT imaging, the tumor-bearing mice were anesthetized by intraperitoneal injection of 100 μL of 10% chloral hydrate. Then, the UCNPs–$Cu_{2-x}S$ nanocomposites (Yb concentration = 0.20 mmol kg^{-1}) were intravenously injected for CT imaging. *In vitro* and *in vivo* CT images were collected using a Philips 256-slice CT scanner. The parameters were as follows: 120 kVp, 300 mA; thickness, 0.9 mm; pitch, 0.99; field of view, 350 mm; gantry rotation time, 0.5 s; table speed, 158.9 mm s^{-1}.

For *in vitro* MR imaging, different concentrations of the UCNPs–$Cu_{2-x}S$ nanocomposite solution (0, 0.4, 0.8, 1.6, and 3.2 mM) were prepared, and then the MR signals were measured by a 3T clinical MRI scanner. For *in vivo* MR imaging, the tumor-bearing mice were anesthetized by intraperitoneal injection of 100 μL of 10% chloral hydrate. Then, the UCNPs–$Cu_{2-x}S$ nanocomposites (Cu concentration = 10 mg kg^{-1}, 150 μL) were intravenously injected for MR imaging.

In vivo synergistic enhanced chemodynamic/photothermal therapy

When the tumor volume had reached about 100 mm^3, the tumor-bearing mice were randomly divided into four groups (n = 6) as follows: (1) control group (5% glucose solution, 200 μL), (2) 1064 nm laser only group (1.0 W cm^{-2}, 6 min), (3) UCNPs–$Cu_{2-x}S$ group (Cu concentration = 10 mg kg^{-1}, 200 μL), and (4) UCNPs-$Cu_{2-x}S$ (Cu concentration = 10 mg kg^{-1}, 200 μL) plus 1064 nm laser (1.0 W cm^{-2}, 6 min) group. During the NIR irradiation, an infrared thermal camera was used to monitor the temperature changes of the tumor sites. The tumor size and body weight of the mice before and after treatment were measured using a caliper and an electronic balance, respectively. The tumor volume can be calculated according to the normal equation (volume = width^2 × length/2). The relative tumor volume was calculated as V/V_0, where the V_0 was the corresponding tumor volume before the treatment. After 14 days, the tumors were dissected and weighed to evaluate the therapeutic efficacy.

Histology analysis

For the *in vivo* toxicity studies, healthy Balb/c mice were injected with 100 μL of UCNPs–$Cu_{2-x}S$ at a dosage of 10 mg kg^{-1} Cu. The mice without any treatment were used as the blank control. Over 30 days, the mice were killed, and the main organs of the mice (heart, liver, spleen, lung, and kidney) were harvested and fixed using 4% paraformaldehyde. Tissue samples were then embedded in paraffin, sliced, and stained using H&E. The histological sections were observed under an optical microscope.

Results and discussion

Synthesis and characterization of UCNPs-$Cu_{2-x}S$ nanocomposites

The multistep synthesis process of the UCNPs–$Cu_{2-x}S$ nanocomposites is shown in Scheme 1. First, $NaYF_4$:Yb/Er core nanoparticles were synthesized through a solvothermal process and

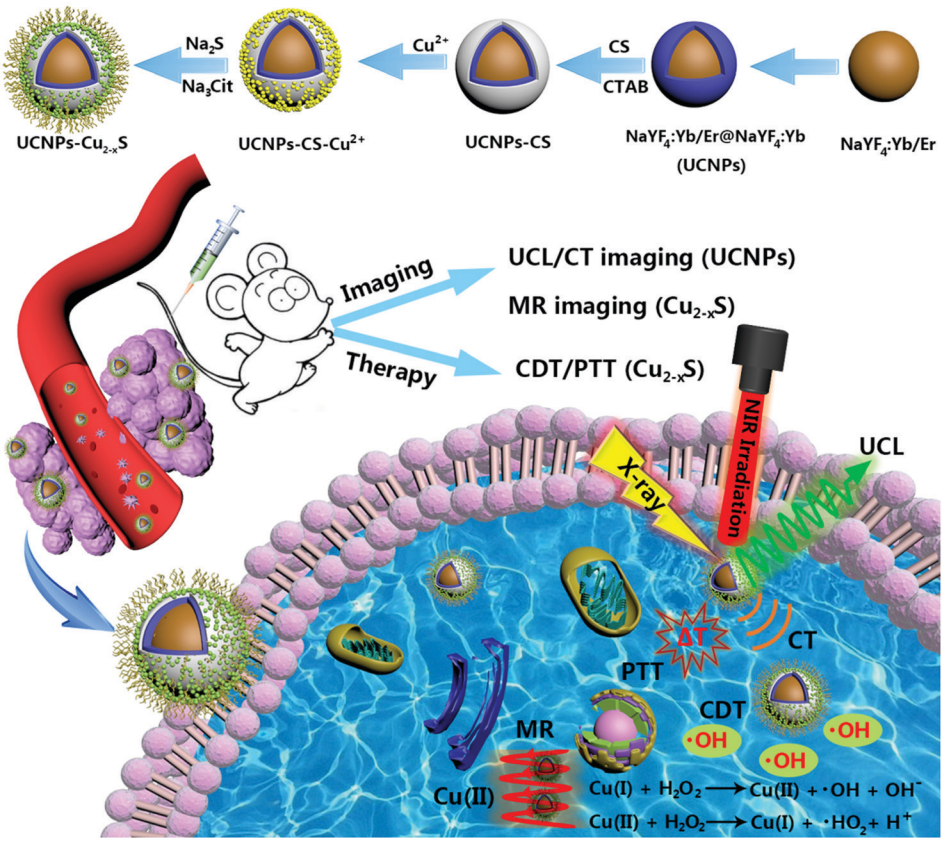

Scheme 1 Schematic illustration of the fabrication process of UCNPs–$Cu_{2-x}S$ nanocomposites, and UCNPs–$Cu_{2-x}S$ nanocomposites for the multimodal imaging guided CDT/PTT of cancer.

then the active shell ($NaYF_4$:Yb) was coated on the core nanoparticles to enhance their UCL intensity and give them a higher CT imaging capability. Subsequently, CS was coated on the surface of the $NaYF_4$:Yb/Er@$NaYF_4$ nanoparticles (UCNPs) with the assistance of CTAB. The water solubility and dispersibility of the UCNPs was significantly improved by modification with the CS layer. Moreover, the CS layer can act as a medium to connect the $Cu_{2-x}S$ nanodots owing to the chelation between glucosamine groups and Cu^{2+} ions. Finally, the sulfur source and stabilizer were added and ultrasmall $Cu_{2-x}S$ nanodots were well decorated and distributed on the surface of the UCNPs. Taken together, the facile synthesis and the excellent multimodal imaging and anti-tumor performance allow the UCNPs–$Cu_{2-x}S$ nanocomposites to be a promising candidate for imaging-guided cancer therapy.

The TEM image of OA-capped $NaYF_4$:Yb/Er core nanoparticles with a mean size of 38.1 ± 0.7 nm are shown in Fig. 1a. The average size of the core/shell $NaYF_4$:Yb/Er@$NaYF_4$:Yb nanoparticles is about 52.5 ± 0.6 nm after further epitaxial growth (Fig. 1b). As shown in Fig. 1c, there is substantially no change in the morphology and size of the UCNPs after coating with CS, and the CS-coated UCNPs nanoparticles (53.8 ± 0.8 nm) with good monodispersity could be well dispersed in water for several weeks. It can be clearly observed from Fig. 1d that spherical $Cu_{2-x}S$ nanodots with a small size of 5.2 ± 0.4 nm are firmly conjugated and grow uniformly on the surface of the UCNPs. Furthermore, the corresponding high-resolution TEM (HRTEM) image (Fig. S1, ESI†) shows clear lattice fringes of UCNPs–$Cu_{2-x}S$ nanocomposites. The interplanar spacing of 0.52 nm matches well with the (100) plane of β-$NaYF_4$ and that of 0.30 nm can be attributed to the (102) plane of CuS, indicating the high crystallinity of the nanocomposites. The bright-field TEM image and the corresponding elemental mapping images (Fig. 1e and f) clearly prove the actual distribution of the Y, Yb, Cu and S elements in the UCNPs–$Cu_{2-x}S$ nanocomposites. Fig. S2 (ESI†) shows the XRD pattern of $NaYF_4$:Yb/Er, $NaYF_4$:Yb/Er@$NaYF_4$:Yb and the UCNPs–$Cu_{2-x}S$ nanocomposites. In the XRD patterns of $NaYF_4$:Yb/Er (black line) and $NaYF_4$:Yb/Er@$NaYF_4$:Yb (blue line), the diffraction peaks can be readily indexed to the characteristic peaks of standard hexagonal $NaYF_4$ (JCPDS no. 16-0334). For the UCNPs–$Cu_{2-x}S$ nanocomposites (red line), the diffraction peaks match very well with the characteristic peaks of the CuS phases (JCPDS card no. 06-0464), Cu_2S phases (JCPDS No. 33-0492) and hexagonal $NaYF_4$ (JCPDS card no. 16-0334). X-ray photoelectron spectroscopy (XPS) (Fig. S3, ESI†) and energy-dispersive X-ray (EDX) spectra (Fig. S4, ESI†) of the UCNPs–$Cu_{2-x}S$ nanocomposites were obtained to confirm the existence of the Na, F, Y, Yb, Er, Cu and S elements. Moreover, from XPS of Cu 2p (Fig. 1g), the peaks of 935.6 eV and 955.3 eV are attributed to Cu^{2+} $2p_{3/2}$ and $2p_{1/2}$, and the peak located at the binding energy of 933.4 eV can

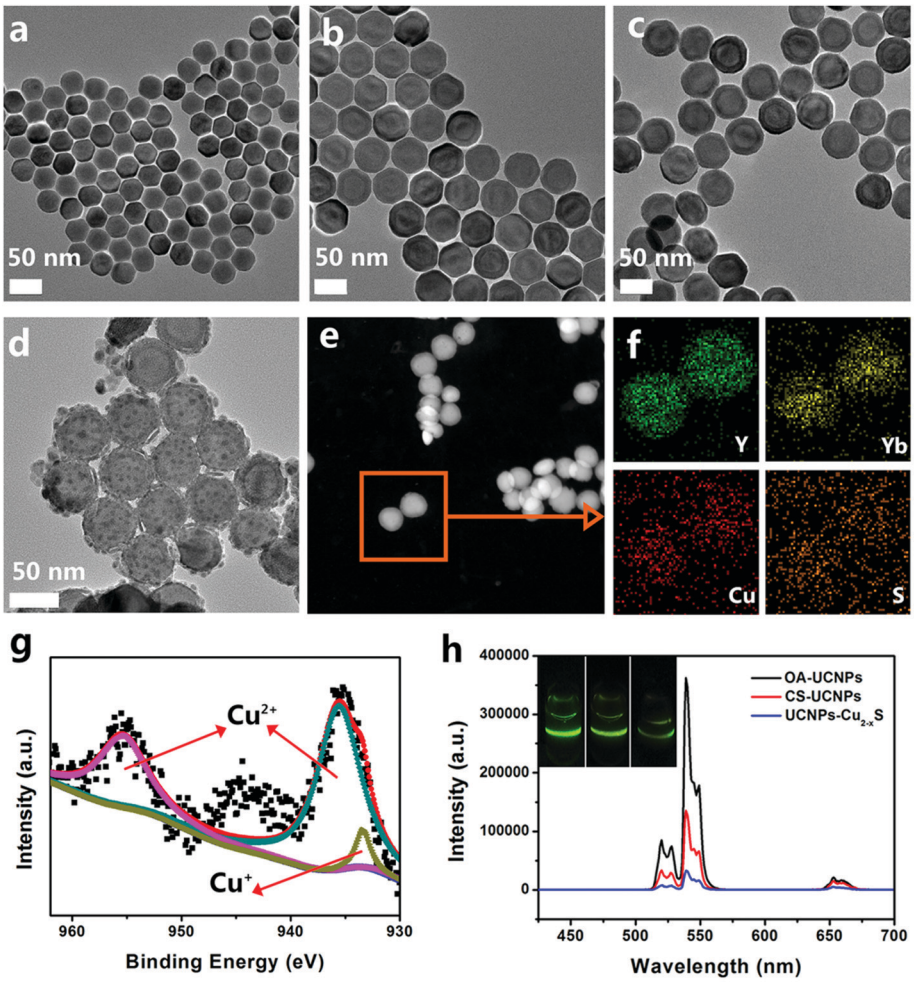

Fig. 1 TEM images of (a) $NaYF_4$:Yb/Er, (b) $NaYF_4$:Yb/Er@$NaYF_4$:Yb (UCNPs), (c) CS-UCNPs, and (d) UCNPs–$Cu_{2-x}S$. (e) HAADF-STEM image of UCNPs–$Cu_{2-x}S$ and (f) the corresponding element mappings. (g) XPS of Cu in UCNPs–$Cu_{2-x}S$. (h) UCL spectra of OA-UCNPs, CS-UCNPs, and UCNP–$Cu_{2-x}S$ excited by a 980 nm NIR laser. Insets are the corresponding digital photographs of the solutions irradiated by the 980 nm NIR laser.

be attributed to Cu^+ $2p_{3/2}$, which indicate the valence state of Cu in the synthesized UCNPs–$Cu_{2-x}S$ nanocomposites is between +1 and +2. The above results fully demonstrate the successful synthesis of the nanocomposites.

To study the luminescent properties of the obtained samples, we measured the UCL spectra of OA-UCNPs, CS-UCNPs and UCNPs–$Cu_{2-x}S$ under 980 nm laser excitation. The emission spectrum of $NaYF_4$:Yb/Er core and $NaYF_4$:Yb/Er@$NaYF_4$:Yb core–shell nanoparticles with characteristic bands at 521, 540 and 655 nm are shown in Fig. S5 (ESI†) and the three distinct characteristic sharp UC emission peaks can be assigned to the $^2H_{11/2} \rightarrow {}^4I_{15/2}$, $^4S_{3/2} \rightarrow {}^4I_{15/2}$ and $^4F_{9/2} \rightarrow {}^4I_{15/2}$ transitions of Er^{3+}, respectively.[45,46] It could be seen that the emission intensity of the $NaYF_4$:Yb/Er@$NaYF_4$:Yb core–shell nanoparticles has been increased by 4.8 times compared with the $NaYF_4$:Yb/Er core nanoparticles. As shown in Fig. 1h, the UCL intensity clearly decreased both in the green and red areas when OA-coated UCNPs were transferred to the hydrophilic phase after coating with a layer of CS; meanwhile, the corresponding green/red ratio was changed from 14.36 in the organic phase to 7.45 in aqueous solution. The UCL intensity of the CS-UCNPs is further decreased by linking the $Cu_{2-x}S$ nanodots, which can be attributed to the nonspecific absorbance of $Cu_{2-x}S$ nanodots. As shown in Fig. S6 (ESI†), the UCL spectrum of the CS-UCNPs was covered by the absorption of the UCNPs–$Cu_{2-x}S$ nanocomposites, resulting in the luminescence resonance energy transfer (LRET) process. In addition, naked-eye-visible UCL photographs of the OA-UCNPs, CS-UCNPs and UCNPs–$Cu_{2-x}S$ nanocomposites are shown in the inset of Fig. 1h. It is noteworthy that the UCNPs–$Cu_{2-x}S$ nanocomposites still possess bright green emission under 980 nm laser irradiation. What is more, the synthetic nanocomposites with the bright UCL emission are promising candidates as bioimaging probes.

Photothermal conversion performance and PT-enhanced catalytic performance of the UCNPs–$Cu_{2-x}S$ nanocomposites

As presented in Fig. 2a, the UCNPs–$Cu_{2-x}S$ nanocomposites show a broad UV-vis-NIR absorption in 400–1200 nm region. It can be observed that the absorption spectrum intensity of UCNPs–$Cu_{2-x}S$ was enhanced steadily with increasing Cu concentration.

The color of the solution changed from colorless to dark green (Fig. S7, ESI†). At the same time, the absorbance values at 808 nm and 1064 nm show a good linear relationship with the Cu concentration, which indicates that the nanocomposites have good dispersibility in water (Fig. S8, ESI†). The nanocomposites have a higher absorption value in the NIR II region than in the NIR I region. Then, the photothermal performance of the UCNPs–$Cu_{2-x}S$ nanocomposites was investigated by monitoring the temperature of the UCNPs–$Cu_{2-x}S$ nanocomposites solution under the irradiation with an 808 nm and a 1064 nm laser (1.0 W cm^{-2}, 10 min), respectively. The temperature of the UCNPs–$Cu_{2-x}S$ nanocomposites solution with different concentrations exhibited an obvious concentration-dependent photothermal conversion behavior (Fig. 2b and Fig. S9, ESI†). It is noteworthy that the temperature of the UCNPs–$Cu_{2-x}S$ nanocomposites solution (12.5, 25, 50, 100, and 200 μg mL^{-1}) could be increased rapidly in the first six minutes and then the temperature grew slowly until it reached a plateau. The temperature change (ΔT) in 10 min is shown in Fig. S10 (ESI†), where the temperature of the UCNPs–$Cu_{2-x}S$ aqueous solution (200 μg mL^{-1}) could reach 52 °C under 1064 nm laser irradiation; however, it only rose to about 42 °C when irradiated with the 808 nm laser under the same conditions. Meanwhile, the IR thermal images of the UCNPs–$Cu_{2-x}S$ aqueous solution (200 μg mL^{-1}) and pure water exposed to 808 nm or 1064 nm lasers are vividly displayed in Fig. 2c. According to the obtained data (Fig. 2d and Fig. S11, ESI†), the photothermal conversion efficiency (η) values were calculated to be 39.3% at 808 nm and 43.8% at 1064 nm, indicating that the UCNPs–$Cu_{2-x}S$ nanocomposites have a noticeable advantage in the NIR II region compared with the NIR I region. The detailed calculation is presented in the experimental section using the reported method. Moreover, the η value of the UCNPs–$Cu_{2-x}S$ nanocomposites was higher than most of the reported photothermal agents, such as UCNPs–Bi_2Se_3 nanocomposites (29.9%),[47] Gd:CuS@BSA NPs (32.3%),[48] $Cu_{2-x}S$ nanodots (30.8%),[30] UCNPs@Au-DOX nanocomposites (12%),[19] and Au-$Cu_{2-x}Se$ heterogeneous nanocrystals (32%).[49] The results indicate that the UCNPs–$Cu_{2-x}S$ nanocomposites with an excellent photothermal capability could efficiently convert NIR light energy into heat. Satisfactorily, the high photothermal conversion efficiency can help reduce the dose of photothermal agent used in future cancer treatment. It is worth noting that the high photothermal stability of photothermal agents is an indispensable condition in the photothermal therapy process. As shown in Fig. S12 and S13 (ESI†), the UV-vis-NIR absorbance spectrum did not change significantly and the color of the solution showed no distinct change before and after 1 h of laser irradiation (808 nm or 1064 nm, 1.0 W cm^{-2}). In addition, when the UCNPs–$Cu_{2-x}S$ nanocomposites solution (200 μg mL^{-1}) was exposed to a 1064 nm laser, the cycle of irradiation/cooling was repeated for four times, and the temperature change was constant (Fig. S14, ESI†). These results demonstrate the excellent photothermal stability of the UCNPs–$Cu_{2-x}S$ nanocomposites. Thus, UCNPs–$Cu_{2-x}S$ nanocomposites could be used as PT agent in the NIR-II biowindow for future cancer therapy.

As is known, Cu(I) can efficiently catalyze H_2O_2 to generate highly toxic •OH by the Fenton-like reaction, which is the critical step in CDT. A methylene blue (MB) degradation experiment was performed to demonstrate the •OH production capacity of the UCNPs–$Cu_{2-x}S$ nanocomposites. When MB was incubated with the UCNPs–$Cu_{2-x}S$ nanocomposites (Cu concentration = 200 μg mL^{-1},

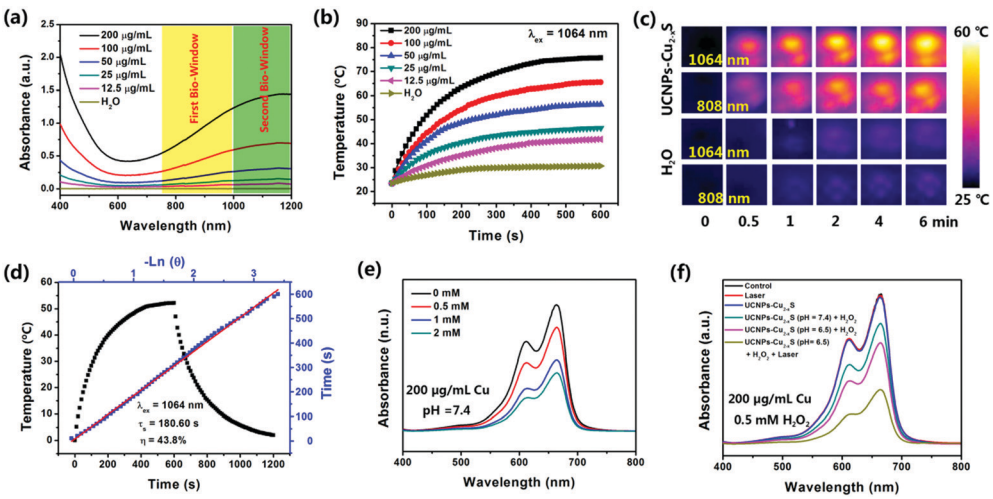

Fig. 2 (a) UV-vis-NIR absorption spectra of UCNPs–$Cu_{2-x}S$ nanocomposites in water at different concentrations (0, 12.5, 25, 50, 100, and 200 μg mL^{-1}). Inset: The first near-infrared biowindow (NIR-I) and the second near-infrared biowindow (NIR-II). (b) Temperature elevation of water and UCNPs–$Cu_{2-x}S$ aqueous solutions at different concentrations as a function of irradiation time exposure to a 1064 nm NIR laser (1.0 W cm^{-2}). The temperature was measured every 10 s using a thermocouple microprobe. (c) Infrared thermal images of the UCNPs–$Cu_{2-x}S$ nanocomposites (Cu concentration = 200 μg mL^{-1}) aqueous solution and pure water irradiated with 808 nm or 1064 nm lasers (1.0 W cm^{-2}) for 6 min. (d) Calculation of the photothermal-conversion efficiency at 1064 nm (NIR-II). Black line: The photothermal response of the UCNPs–$Cu_{2-x}S$ aqueous solution (200 μg mL^{-1}) for 600 s with a NIR-II laser before the laser was shut off. Red line: linear time data *versus* $-\ln\theta$ obtained from the cooling period. (e) MB degradation by •OH generated by UCNPs–$Cu_{2-x}S$ nanocomposites (Cu concentration = 200 μg mL^{-1}, pH = 7.4) plus different concentrations of H_2O_2. (f) MB degradation caused by •OH production after receiving different treatments (Cu concentration = 200 μg mL^{-1}, 0.5 mM H_2O_2).

pH = 7.4) and different concentrations of H_2O_2 for 10 minutes, the absorption intensity of MB will decrease significantly as the concentration of H_2O_2 increases (Fig. 2e). As shown in Fig. 2f, the absorbance of MB shows a higher decrease in acidic conditions (pH = 6.5) compared with the same treatment in physiological buffer solution (pH = 7.4). Moreover, the absorption value will be further greatly reduced under laser irradiation (1064 nm, 10 min), which indicates that hyperthermia caused by laser irradiation could effectively promote the production of •OH. However, there was no apparent change in the absorption value of MB for only UCNPs–$Cu_{2-x}S$ solution or the laser-only group. The above excellent results, including the high photothermal conversion efficiency and good PT-enhanced catalytic performance, indicate that the UCNPs–$Cu_{2-x}S$ nanocomposites hold great prospects as a promising candidate for both PTT and PT-enhanced CDT.

Cytotoxicity assessment and synergistic enhanced CDT/PTT of UCNPs–$Cu_{2-x}S$ nanocomposites *in vitro*

As shown in Fig. 3a, the potential cytotoxicity of the UCNPs–$Cu_{2-x}S$ nanocomposites was first evaluated by a standard CCK-8 assay, and the viabilities of HeLa cells (cervical cancer cells) were maintained up to 93.7% after incubation with various concentrations of UCNPs–$Cu_{2-x}S$ nanocomposites for 24 h. The results show almost no obvious cytotoxicity to HeLa cells for UCNPs–$Cu_{2-x}S$ nanocomposites in solutions with a Cu concentration ranging from 0 to 200 μg mL^{-1}. Inspired by the desirable property of the UCNPs–$Cu_{2-x}S$ nanocomposites of a high photothermal conversion capacity and a PT-enhanced catalytic performance to generate •OH, the *in vitro* synergistic therapeutic efficiency of the UCNPs–$Cu_{2-x}S$ nanocomposites against HeLa cells was first evaluated using the CCK-8 assay. As shown in

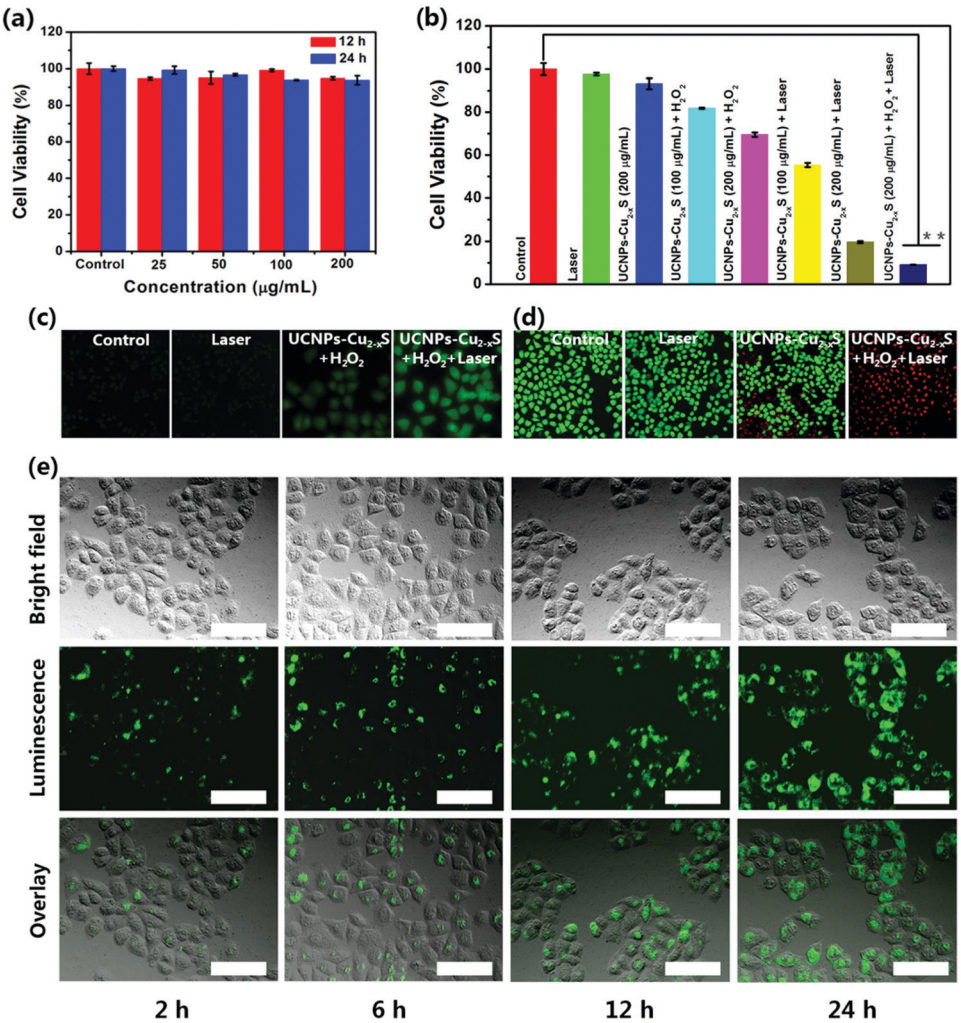

Fig. 3 (a) Viability of HeLa cells after incubation with UCNPs–$Cu_{2-x}S$ at varying concentrations (0–200 μg mL^{-1}) for 12 h and 24 h. (b) CCK-8 assay of HeLa cells treated in different groups, $^{**}p < 0.01$ (two-tailed *t* test). (c) Fluorescence microscopy images of HeLa cells stained by DCFH-DA in different groups: control, laser, UCNPs–$Cu_{2-x}S$ + H_2O_2 and UCNPs–$Cu_{2-x}S$ + H_2O_2+ laser; scale bars are 20 μm. (d) Fluorescence microscopy images of HeLa cells co-stained with calcein AM (live cells, green) and PI (dead cells, red) after different treatments: control, laser, CNPs–$Cu_{2-x}S$ + H_2O_2 and UCNPs–$Cu_{2-x}S$ + H_2O_2 + laser; scale bars are 50 μm. (e) Inverted fluorescence microscope images of HeLa cells incubated with UCNPs–$Cu_{2-x}S$ for 2 h, 6 h, 12 h and 24 h at 37 °C. Each series can be classified into the bright field image, luminescence image and overlay of the above two. The scale bar in each image is 50 μm.

Fig. 3b, the viability of HeLa cells treated with UCNPs–$Cu_{2-x}S$ + laser and UCNPs–$Cu_{2-x}S$ + H_2O_2 was calculated to be 19.6% and 69.5%. Specifically, a higher therapeutic effect can be observed when the HeLa cells are treated with UCNPs–$Cu_{2-x}S$ + H_2O_2 + laser, where the cell inhibition rate can be as high as 91%. We then evaluated the synergetic enhanced CDT/PTT of the UCNPs–$Cu_{2-x}S$ nanocomposites *in vitro*. The ability of the UCNPs–$Cu_{2-x}S$ nanocomposites to generate $^{\bullet}OH$ at the cellular level was verified using 2,7-dichlorofluorescin diacetate (DCFH-DA). As shown in Fig. 3c, almost no obvious fluorescence signal was observed in the control group and the 1064 nm laser group. Fluorescence enhancement can be observed when the HeLa cells are treated with UCNPs–$Cu_{2-x}S$ + H_2O_2, demonstrating that Cu(I) could consume H_2O_2 to generate $^{\bullet}OH$. As expected, a higher fluorescence signal could be detected in the UCNPs–$Cu_{2-x}S$ + H_2O_2 + laser group compared with the UCNPs–$Cu_{2-x}S$ + H_2O_2 group, suggesting that the excellent photothermal effect of the UCNPs–$Cu_{2-x}S$ nanocomposites under the irradiation of a 1064 nm laser could greatly promote the production efficiency of $^{\bullet}OH$. To further confirm the *in vitro* anticancer effect of the UCNPs–$Cu_{2-x}S$ nanocomposites, live/dead cell staining assays were performed by staining HeLa cells with calcein acetoxymethyl ester (AM) and propidium iodide (PI), and the fluorescence microscopy images are shown in Fig. 3d. Almost no obvious cytotoxicity is seen for the control group and the 1064 nm laser group (green fluorescence). Compared with the UCNPs–$Cu_{2-x}S$ + H_2O_2 group, the HeLa cells treated with UCNPs–$Cu_{2-x}S$ + H_2O_2 under 1064 nm irradiation showed severe apoptosis and nearly all of the cells are killed, exhibiting a red fluorescence in the entire well region, which indicates that PT-enhanced CDT and PTT have a significant therapeutic effect. These findings at the cellular level effectively demonstrate that the UCNPs–$Cu_{2-x}S$ nanocomposites with an outstanding photothermal ablation effect and PT-enhanced CDT could be applied as a promising candidate for cancer treatment.

UCL imaging properties of UCNPs–$Cu_{2-x}S$ nanocomposites *in vitro* and *in vivo*

The *in vitro* UCL imaging of the UCNPs–$Cu_{2-x}S$ nanocomposites was visualized by the modified inverted fluorescence microscope. For the UCL imaging assay, HeLa cells were incubated with UCNPs–$Cu_{2-x}S$ nanocomposites and the UCL images were recorded at different time intervals. As presented in Fig. 3e, an evident green luminescence signal was observed in HeLa cells after incubation with the UCNPs–$Cu_{2-x}S$ nanocomposites at 37 °C for 2 h, 6 h, 12 h and 24 h. Meanwhile, the obviously enhanced UCL signal indicates that more and more nanoparticles are incubated into the HeLa cells over the course of the incubation time. Moreover, corresponding time-dependent UCL spectra of HeLa cells incubated with UCNPs–$Cu_{2-x}S$ nanocomposites are shown in Fig. S15 (ESI†). This result forcefully demonstrates that the UCNPs–$Cu_{2-x}S$ nanocomposites can be taken up by HeLa cells and could be used as an excellent UCL signal probe for cell imaging. Encouraged by the surprising results *in vitro*, UCL imaging was then evaluated in Balb/c mice. The UCNPs–$Cu_{2-x}S$ was intratumorally injected into the U14 tumor-bearing mice. As shown in Fig. S16 (ESI†), the bright green UCL signal in the tumor site was observed under 980 nm laser irradiation. Thus, the UCNPs–$Cu_{2-x}S$ nanocomposites hold great promise for improving the early detection of cancer.

In vitro and *in vivo* X-ray CT imaging and MR imaging

As is known, X-ray CT imaging is a valuable and noninvasive medical imaging technique which can provide excellent image resolution and deep tissue penetration, and it has been extensively applied for modern clinical diagnosis and prognosis. The X-ray attenuation coefficient was determined by the atomic number and electron density of the CT contrast agent.[38] Ytterbium (Z = 70, 6.98 g cm^{-3}) has a higher atomic number and electron density compared with the extensively applied iobitridol contrast agent (Z = 53, 4.9 g cm^{-3}), which endows UCNPs–$Cu_{2-x}S$ nanocomposites with great potential in X-ray CT imaging. To assess the *in vitro* CT contrast efficacy, the X-ray absorption coefficient of the UCNPs–$Cu_{2-x}S$ nanocomposites was investigated and compared with that of iobitridol. As shown in Fig. 4a, the brightness of the CT signal of both contrast agents was enhanced with increasing their concentrations, which could be intuitively observed in the pseudo-color image. Meanwhile, the HU values exhibited good linear dependence on the concentrations of both contrast agents (Fig. 4b). The HU value of the UCNPs–$Cu_{2-x}S$ nanocomposites (260.6 HU) is higher than that of iobitridol (137.1 HU) at the same concentration. These results confirmed that the UCNPs–$Cu_{2-x}S$ nanocomposites have a superior X-ray CT imaging ability and could be applied as a promising CT contrast agent. Subsequently, the feasibility of the UCNPs–$Cu_{2-x}S$ nanocomposites as a CT contrast agent *in vivo* was assessed. The time-dependent CT imaging of the UCNPs–$Cu_{2-x}S$ nanocomposites in the U14 tumor-bearing mice after intravenous injection was studied. As shown in Fig. 4c, the CT signal at the tumor site was obviously enhanced within 2 h due to the enhanced permeability and retention (EPR) effect. It can be observed that the CT signal of the tumor site is significantly reduced after 24 h post-injection, indicating the gradual excretion of the UCNPs–$Cu_{2-x}S$ nanocomposites from mice. These desirable results indicate that the UCNPs–$Cu_{2-x}S$ nanocomposites could serve as a promising CT contrast agent *in vivo*.

Furthermore, time tracking of the *in vivo* CT imaging of the UCNPs–$Cu_{2-x}S$ nanocomposites (Yb concentration = 0.20 mmol kg^{-1}) was carried out to investigate the biodistribution of the UCNPs–$Cu_{2-x}S$ nanocomposites. Fig. S17 (ESI†) shows the CT imaging of major organs (heart, liver, spleen, kidney) at different time points (0, 10 min, 30 min, 1 h, 2 h, 24 h). In the first 2 h after intravenous injection, the UCNPs–$Cu_{2-x}S$ nanocomposites were mainly distributed in the organs of the reticuloendothelial system, such as the liver and spleen, followed by the heart and kidney. Fig. S18 (ESI†) shows the change in the HU values of these organs over time. With the increase of time, the CT signals of all tested organs were observed to weaken, which indicates that the UCNPs–$Cu_{2-x}S$ nanocomposites are gradually excreted from the mice.

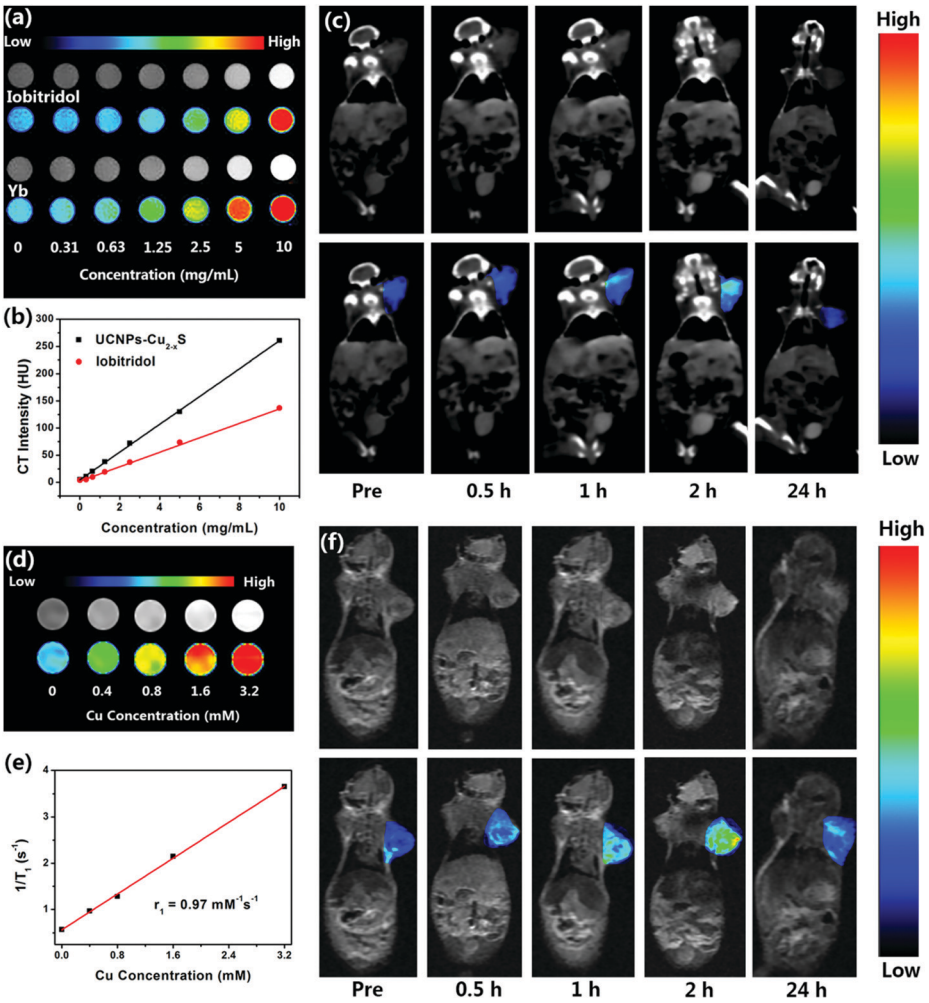

Fig. 4 (a) *In vitro* CT images of iobitridol and UCNPs–$Cu_{2-x}S$ nanocomposites at different concentrations. (b) Concentration-dependent CT signals of iobitridol (red line) and UCNPs–$Cu_{2-x}S$ nanocomposites (black line) *in vitro*. (c) Time-dependent CT imaging in tumor-bearing mice before and after intravenous injection of the UCNPs–$Cu_{2-x}S$ nanocomposites. (d) *In vitro* MR images of the UCNPs–$Cu_{2-x}S$ nanocomposites with different Cu concentrations. (e) The linear relationship between the T_1-MR signal and different Cu concentrations. (f) Time-dependent MR imaging in tumor-bearing mice before and after intravenous injection of the UCNPs–$Cu_{2-x}S$ nanocomposites.

Due to the presence of paramagnetic Cu(II) in the UCNPs–$Cu_{2-x}S$ nanocomposites, it can be used as an effective T_1-weighted MRI contrast agent. Encouragingly, with the increase of UCNPs–$Cu_{2-x}S$ concentration, the acquired MR images gradually turned brighter in the Cu concentration range from 0 to 3.2 mM under T_1-weighted mode (Fig. 4d). The T_1 relaxivity coefficient (r_1) value of UCNPs–$Cu_{2-x}S$ was measured to be 0.97 mM^{-1} s^{-1} (Fig. 4e). These results suggest that the UCNPs–$Cu_{2-x}S$ nanocomposites show great potential for MR imaging. Then, *in vivo* T_1-weighted MR imaging was evaluated in Balb/c mice bearing U14 tumors. As displayed in Fig. 4f, the MR signal at the tumor site gradually brightened and showed a marked positive enhancement after intravenous injection of the UCNPs–$Cu_{2-x}S$ nanocomposites within 2 h, and then the signal decreased until 24 h post-injection due to metabolism of a portion of the UCNPs–$Cu_{2-x}S$ nanocomposites, which is consistent with the aforementioned CT imaging results. These desirable results demonstrate the capability of the UCNPs–$Cu_{2-x}S$ nanocomposites to serve as a contrast agent for T_1 weighted MR imaging.

Synergistic chemodynamic/photothermal therapy and long-term toxicity *in vivo*

Compared with the NIR I window, NIR II window has a more ideal laser penetration depth and a better maximum allowable exposure, which is more attractive for photothermal treatment of deeply buried tumors.[50–52] The results of the *in vitro* photothermal effect indicate that the UCNPs–$Cu_{2-x}S$ nanocomposites have a more ideal absorption rate and a higher photothermal conversion efficiency in the NIR II biowindow. Encouraged by the considerable PT effect in the NIR II biowindow and PT-enhanced CDT, we evaluated the synergistic therapeutic effect of the UCNPs–$Cu_{2-x}S$ nanocomposites triggered by a 1064 nm laser *in vivo*. Based on the results of CT and MR imaging, photoinduced synergistic cancer therapy was performed 2 h after

intravenous injection of UCNPs–$Cu_{2-x}S$ nanocomposites and infrared thermal camera was used to monitor the real-time temperature of tumor site. As shown in Fig. 5a, the temperature of the tumor site increased rapidly under 1064 nm laser irradiation whereas the temperature of the tumor site in the control group did not change significantly. As shown in Fig. 5b, the temperature of the tumor could be raised to 56 °C in the presence the UCNPs–$Cu_{2-x}S$ nanocomposites under 1064 nm laser irradiation (1.0 W cm^{-2}, 6 min). However, the temperature of the tumor regions in the control group exhibited a minor elevation. The above results demonstrate that the UCNPs–$Cu_{2-x}S$ nanocomposites could be applied as an excellent PTT agent for tumor ablation *in vivo*. To verify the treatment effect, Balb/c mice bearing U14 cells were randomly divided into four groups ($n = 6$): (1) control group; (2) laser-only group; (3) UCNPs–$Cu_{2-x}S$ group (CDT); and (4) UCNPs–$Cu_{2-x}S$ + laser group (PT-enhanced CDT/PTT). The tumor for the mice was irradiated for 6 min by a 1064 nm laser after 2 h injection of the UCNPs–$Cu_{2-x}S$ nanocomposites. The change of tumor volume and body weight of the mice was measured every 2 d over a period of 14 days. As seen in Fig. 5c, the body weight of the mice maintained a steady growth during the treatment. As shown in Fig. 5d–f, the tumor volume shows a rapid growth trend for the control and laser groups; meanwhile, the tumor treated with UCNPs–$Cu_{2-x}S$ has been suppressed to some extent, which indicates that CDT has a certain therapeutic effect, but the single treatment cannot completely eliminate the tumor. When the mice were treated with UCNPs–$Cu_{2-x}S$ + laser, the tumor volume

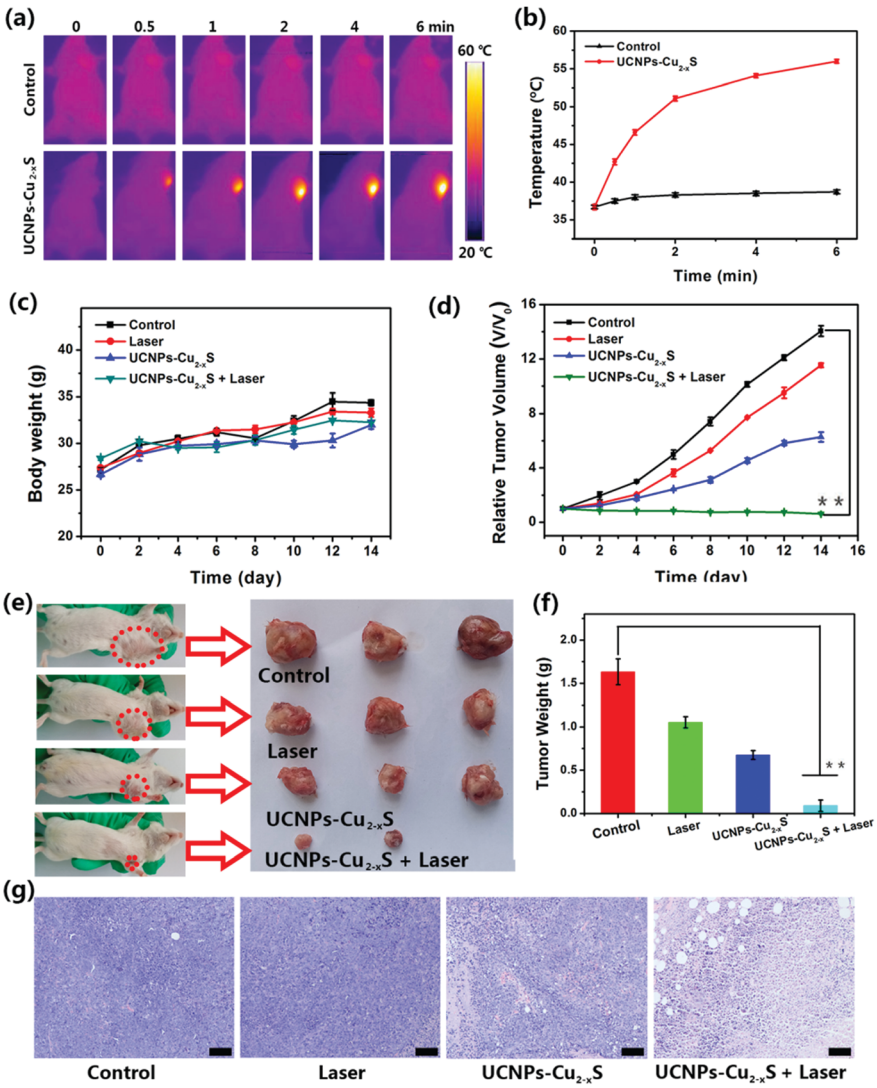

Fig. 5 (a) Infrared thermal images of the tumor site of tumor-bearing mice intravenously injected with 5% glucose solution (control) and UCNPs–$Cu_{2-x}S$ nanocomposites followed by 1064 nm laser irradiation for 6 min. (b) Corresponding temperature change curves at the tumor sites based on thermal images. (c) Body weight of mice under different treatments. (d) Relative tumor growth curves of different groups after various treatments, $^{**}p < 0.01$ (two-tailed *t*-test). (e) The digital photographs of excised tumors from representative euthanized mice and (f) mean tumor weight of each group after various treatments from the last day of the experiment (day 14), $^{**}p < 0.01$ (two-tailed *t*-test). (g) H&E-stained slices of tumor tissues collected from different groups. All scale bars are 100 μm.

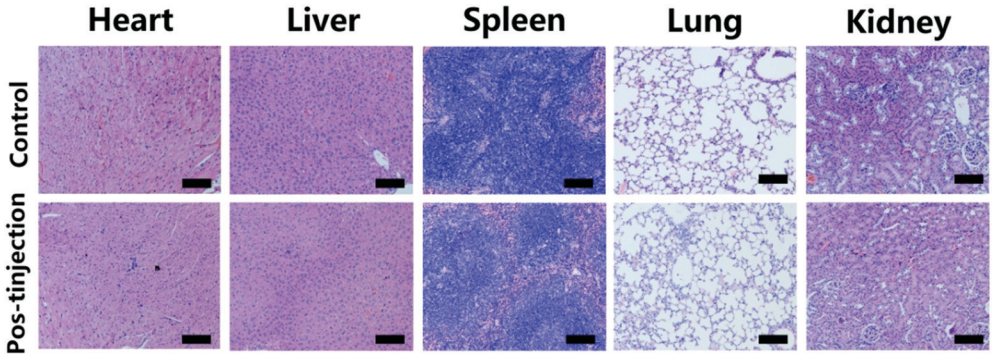

Fig. 6 H&E stained images of major organs (heart, liver, spleen, lung, and kidney) of mice 30 days post-injection of UCNPs–$Cu_{2-x}S$ nanocomposites. All scale bars are 100 μm.

could be effectively suppressed and even completely eliminated without any regrowth, owing to hyperthermia in the tumor site caused by the photothermal effect and the large amount of toxic •OH produced by the PT-enhanced CDT effect. Through hematoxylin and eosin (H&E) staining results, it can be observed that the tumor tissue in the treatment group has obvious necrosis (Fig. 5g). The above results indicate that the synergetic effect of CDT/PTT can play an important role in the complete ablation of tumors *in vivo*. Finally, the long-term toxicity of the UCNPs–$Cu_{2-x}S$ nanocomposites to normal organs (heart, liver, spleen, lung, and kidney) was evaluated. All major organs were sliced and stained with H&E after 30 d of injection. Moreover, no appreciable tissue damage and abnormal inflammatory lesions were observed compared with the control group (Fig. 6), indicating that the UCNPs–$Cu_{2-x}S$ nanocomposites, with negligible long-term toxicity *in vivo*, show great potential for effective multimodal imaging guided cancer treatment.

Conclusions

In summary, a novel UCNPs–$Cu_{2-x}S$ nanoplatform has been successfully constructed, which could be used simultaneously for the multi-modal imaging guided synergistic enhanced CDT/PTT of cancer. In this case, spherical $Cu_{2-x}S$ nanodots can be firmly grown *in situ* and well distributed on the surface of the UCNPs. The UCNPs gave the nanocomposites a UCL/CT imaging capability and the $Cu_{2-x}S$ nanodots offered MR imaging capability due to the presence of paramagnetic Cu(II); meanwhile, Cu(I) in the $Cu_{2-x}S$ nanodots could produce a large amount of toxic •OH in response to over-expressed H_2O_2 in the tumor tissue. More importantly, $Cu_{2-x}S$ nanodots offered an outstanding photothermal effect due to strong absorbance in the NIR II window. Furthermore, the UCNPs–$Cu_{2-x}S$ nanocomposites show highly efficient photothermal conversion and an ideal photothermal killing effect in PT-enhanced CDT, together with pronounced upconversion luminescence for UCL imaging toward HeLa cancer cells, as well as an outstanding CT/MR imaging effect *in vitro* and *in vivo*. These results demonstrate that the UCNPs–$Cu_{2-x}S$ nanocomposites could serve as a potential theranostic agent for the simultaneous diagnosis and treatment of cancer. Taken together, the facile growth synthesis, negligible toxicity, high photothermal conversion efficiency, outstanding photothermal killing effect and the multi-modal imaging guided synergistic enhanced CDT/PTT all lay the foundation for the application of UCNPs–$Cu_{2-x}S$ nanocomposites in the field of biomedicine.

Conflicts of interest

There are no conflicts to declare.

Acknowledgements

This work is supported by the financial aid from the National Natural Science Foundation of China (21871248, 21834007, and 22020102003), K. C. Wong Education Foundation (GJTD-2018-09), the International Partnership Program of Chinese Academy of Sciences (121522KYSB20190022), the Youth Innovation Promotion Association of Chinese Academy of Sciences (Y201947), the Key Research Program of Frontier Sciences, CAS (YZDY-SSW-JSC018), and Jilin Province Science and Technology Development Plan Project (20180101172JC).

Notes and references

1 S. Han, A. Samanta, X. Xie, L. Huang, J. Peng, S. J. Park, D. B. L. Teh, Y. Choi, Y.-T. Chang, A. H. All, Y. Yang, B. Xing and X. Liu, *Adv. Mater.*, 2017, **29**, 1700244.
2 S. Zhao, R. R. Tian, B. Q. Shao, Y. Feng, S. W. Yuan, L. P. Dong, L. Zhang, K. Liu, Z. X. Wang and H. P. You, *ACS Appl. Mater. Interfaces*, 2019, **11**, 394–402.
3 Q. Xiao, X. Zheng, W. Bu, W. Ge, S. Zhang, F. Chen, H. Xing, Q. Ren, W. Fan, K. Zhao, Y. Hua and J. Shi, *J. Am. Chem. Soc.*, 2013, **135**, 13041–13048.
4 D. Yang, G. Yang, P. Yang, R. Lv, S. Gai, C. Li, F. He and J. Lin, *Adv. Funct. Mater.*, 2017, **27**, 1700371.
5 G. Song, C. Liang, H. Gong, M. Li, X. Zheng, L. Cheng, K. Yang, X. Jiang and Z. Liu, *Adv. Mater.*, 2015, **27**, 6110–6117.
6 J. J. He, W. Zheng, F. L. Ligmajer, C. F. Chan, Z. Y. Bao, K. L. Wong, X. Y. Chen, J. H. Hao, J. Y. Dai, S. F. Yu and D. Y. Lei, *Light: Sci. Appl.*, 2017, **6**, 11.

7 T. X. Gu, L. Cheng, F. Gong, J. Xu, X. Li, G. R. Han and Z. Liu, *ACS Appl. Mater. Interfaces*, 2018, **10**, 15494–15503.
8 D. Song, S. Y. Chi, X. Li, C. X. Wang, Z. Li and Z. Liu, *ACS Appl. Mater. Interfaces*, 2019, **11**, 41100–41108.
9 Z. Li, X. Qiao, G. He, X. Sun, D. Feng, L. Hu, H. Xu, H.-B. Xu, S. Ma and J. Tian, *Nano Res.*, 2020, **13**, 3377–3386.
10 H. Zhu, Y. Wang, C. Chen, M. Ma, J. Zeng, S. Li, Y. Xia and M. Gao, *ACS Nano*, 2017, **11**, 8273–8281.
11 K. M. Du, P. P. Lei, L. L. Dong, M. L. Zhang, X. Gao, S. Yao, J. Feng and H. J. Zhang, *Appl. Mater. Today*, 2020, **18**, 100497.
12 L. J. Deng, Y. F. Xu, C. X. Sun, B. F. Yun, Q. Sun, C. J. Zhao and Z. Li, *Sci. Bull.*, 2018, **63**, 917–924.
13 P. P. Lei, R. An, X. H. Zheng, P. Zhang, K. M. Du, M. L. Zhang, L. L. Dong, X. Gao, J. Feng and H. J. Zhang, *Nanoscale*, 2018, **10**, 16765–16774.
14 Z. M. Tang, Y. Y. Liu, M. Y. He and W. B. Bu, *Angew. Chem., Int. Ed.*, 2019, **58**, 946–956.
15 Y. Liu, J. Wu, Y. Jin, W. Zhen, Y. Wang, J. Liu, L. Jin, S. Zhang, Y. Zhao, S. Song, Y. Yang and H. Zhang, *Adv. Funct. Mater.*, 2019, **29**, 1904678.
16 L.-S. Lin, T. Huang, J. Song, X.-Y. Ou, Z. Wang, H. Deng, R. Tian, Y. Liu, J.-F. Wang, Y. Liu, G. Yu, Z. Zhou, S. Wang, G. Niu, H.-H. Yang and X. Chen, *J. Am. Chem. Soc.*, 2019, **141**, 9937–9945.
17 W. T. Tang, Z. L. Dong, R. Zhang, X. Yi, K. Yang, M. L. Jin, C. Yuan, Z. D. Xiao, Z. Liu and L. Cheng, *ACS Nano*, 2019, **13**, 284–294.
18 T. Chen, L. Su, X. Ge, W. Zhang, Q. Li, X. Zhang, J. Ye, L. Lin, J. Song and H. Yang, *Nano Res.*, 2020, **13**(18), 3268–3277.
19 R. Wei, W. Xi, H. Wang, J. Liu, T. Mayr, L. Shi and L. Sun, *Nanoscale*, 2017, **9**, 12885–12896.
20 C. Liu, D. Wang, S. Zhang, Y. Cheng, F. Yang, Y. Xing, T. Xu, H. Dong and X. Zhang, *ACS Nano*, 2019, **13**, 4267–4277.
21 Z. Yin, W. Zhang, Q. Fu, H. Yue, W. Wei, P. Tang, W. J. Li, W. Z. Li, L. L. Lin, G. H. Ma and D. Ma, *Small*, 2014, **10**, 3619–3624.
22 Q. S. Wang, H. Wang, Y. Yang, L. H. Jin, Y. Liu, Y. Wang, X. Y. Yan, J. Xu, R. Q. Gao, P. P. Lei, J. J. Zhu, Y. H. Wang, S. Y. Song and H. J. Zhang, *Adv. Mater.*, 2019, **31**, 1904836.
23 X. Bao, Y. Yuan, J. Q. Chen, B. H. Zhang, D. Li, D. Zhou, P. T. Jing, G. Y. Xu, Y. L. Wang, K. Hola, D. Z. Shen, C. F. Wu, L. Song, C. B. Liu, R. Zboril and S. N. Qu, *Light: Sci. Appl.*, 2018, **7**, 11.
24 Q. You, Q. Sun, J. Wang, X. Tan, X. Pang, L. Liu, M. Yu, F. Tan and N. Li, *Nanoscale*, 2017, **9**, 3784–3796.
25 S. Zhang, C. Sun, J. Zeng, Q. Sun, G. Wang, Y. Wang, Y. Wu, S. Dou, M. Gao and Z. Li, *Adv. Mater.*, 2016, **28**, 8927–8936.
26 Z. Li, J. Shao, Q. Luo, X.-F. Yu, H. Xie, H. Fu, S. Tang, H. Wang, G. Han and P. K. Chu, *Biomaterials*, 2017, **133**, 37–48.
27 T. Liu, C. Wang, X. Gu, H. Gong, L. Cheng, X. Shi, L. Feng, B. Sun and Z. Liu, *Adv. Mater.*, 2014, **26**, 3433–3440.
28 L. H. Zhang, Y. Qin, Z. M. Zhang, F. Fan, C. L. Huang, L. Lu, H. Wang, X. Jin, H. X. Zhao, D. L. Kong, C. Wang, H. F. Sun, X. G. Leng and D. W. Zhu, *Acta Biomater.*, 2018, **75**, 371–385.
29 W. Fan, W. Bu and J. Shi, *Adv. Mater.*, 2016, **28**, 3987–4011.
30 R. Hu, Y. Fang, M. Huo, H. Yao, C. Wang, Y. Chen and R. Wu, *Biomaterials*, 2019, **206**, 101–114.
31 L. L. Dong, K. Li, D. Wen, Y. Lu, K. M. Du, M. L. Zhang, X. Gao, J. Feng and H. J. Zhang, *Nanoscale*, 2019, **11**, 12853–12857.
32 D. Pan, S. D. Caruthers, A. Senpan, C. Yalaz, A. J. Stacy, G. Hu, J. N. Marsh, P. J. Gaffney, S. A. Wickline and G. M. Lanza, *J. Am. Chem. Soc.*, 2011, **133**, 9168–9171.
33 S. Y. Han, R. R. Deng, X. J. Xie and X. G. Liu, *Angew. Chem., Int. Ed.*, 2014, **53**, 11702–11715.
34 S. L. Wang, A. Y. Bi, W. B. Zeng and Z. Cheng, *J. Mater. Chem. B*, 2016, **4**, 5331–5348.
35 H. He, C. B. Howard, Y. H. Chen, S. H. Wen, G. G. Lin, J. J. Zhou, K. J. Thurecht and D. Y. Jin, *Anal. Chem.*, 2018, **90**, 3024–3029.
36 J. Zheng, Y. Wu, D. Xing and T. Zhang, *Nano Res.*, 2019, **12**, 931–938.
37 T. Wang, M. Yang, J. Huang, Y. Zhao, H. Wang, S. Leng, J. Chen, G. Sun and J. Liu, *Sci. Bull.*, 2017, **62**, 903–912.
38 Y. Sun, X. Zhu, J. Peng and F. Li, *ACS Nano*, 2013, **7**, 11290–11300.
39 K. M. Du, X. Xu, S. Yao, P. P. Lei, L. L. Dong, M. L. Zhang, J. Feng and H. J. Zhang, *CrystEngComm*, 2018, **20**, 1945–1953.
40 Z. Zhang, M. K. G. Jayakumar, X. Zheng, S. Shikha, Y. Zhang, A. Bansal, D. J. J. Poon, P. L. Chu, E. L. L. Yeo, M. L. K. Chua, S. K. Chee and Y. Zhang, *Nat. Commun.*, 2019, **10**, 4586.
41 G. Y. Chen, H. L. Qju, P. N. Prasad and X. Y. Chen, *Chem. Rev.*, 2014, **114**, 5161–5214.
42 M. Xu, G. Yang, H. Bi, J. Xu, L. Feng, D. Yang, Q. Sun, S. Gai, F. He, Y. Dai, C. Zhong and P. Yang, *Chem. Eng. J.*, 2019, **360**, 866–878.
43 X. Xu, Y. Long, P. Lei, L. Dong, K. Du, J. Feng and H. Zhang, *J. Mater. Chem. C*, 2017, **5**, 9666–9672.
44 K. M. Du, P. P. Lei, M. L. Zhang, X. Gao, S. Yao, C. Y. Li, J. Feng and H. J. Zhang, *Nanoscale*, 2020, **12**, 3977–3987.
45 F. Wang and X. G. Liu, *J. Am. Chem. Soc.*, 2008, **130**, 5642–5643.
46 Y. Wang, K. Zheng, S. Song, D. Fan, H. Zhang and X. Liu, *Chem. Soc. Rev.*, 2018, **47**, 6473–6485.
47 S. Zhao, R. Tian, B. Shao, Y. Feng, S. Yuan, L. Dong, L. Zhang, Z. Wang and H. You, *Chem. – Eur. J.*, 2020, **5**, 1127–1135.
48 W. Yang, W. Guo, W. Le, G. Lv, F. Zhang, L. Shi, X. Wang, J. Wang, S. Wang, J. Chang and B. Zhang, *ACS Nano*, 2016, **10**, 10245–10257.
49 D. Zhu, M. Liu, X. Liu, Y. Liu, P. N. Prasad and M. T. Swihart, *J. Mater. Chem. B*, 2017, **5**, 4934–4942.
50 H. Lin, S. S. Gao, C. Dai, Y. Chen and J. L. Shi, *J. Am. Chem. Soc.*, 2017, **139**, 16235–16247.
51 X. X. Han, J. Huang, X. X. Jing, D. Y. Yang, H. Lin, Z. G. Wang, P. Li and Y. Chen, *ACS Nano*, 2018, **12**, 4545–4555.
52 X. Wang, Y. C. Ma, X. Sheng, Y. C. Wang and H. X. Xu, *Nano Lett.*, 2018, **18**, 2217–2225.

